Low Richardson Number in the Tropical Cyclone Outflow Layer

John Molinari, Patrick Duran, and David Vollaro

Department of Atmospheric and Environmental Sciences, University at Albany,

State University of New York, Albany, New York

Submitted to *Journal of the Atmospheric Sciences*

December 30, 2013

Revised

March 19, 2013

Second revision

May 18, 2014

Corresponding author address:
John Molinari
University at Albany, SUNY
Atmospheric and Environmental Sciences, ES 351
1400 Washington Avenue
Albany, NY 12222

ABSTRACT

Dropsondes from the NOAA G-IV aircraft were used to examine the presence of low bulk Richardson number (R_B) in tropical cyclones. At least one 400-m layer above z = 7.5 km exhibited $R_B < 1$ in 96% of sondes, and $R_B \leq 0.25$ in 35% of sondes. The latter represent almost certain turbulence. Sondes from major Hurricane Ivan (2004) were examined in detail. Turbulent layers fell into three broad groups. The first was found below cloud base near the edge of the central dense overcast (CDO) where relative humidity fell below 40%. Near-zero static stability existed within the turbulent layer with stability and shear maxima above it. This structure strongly resembled that seen previously from sublimation of precipitation beneath cloud base. The second type of turbulent layer was located within CDO clouds in the upper troposphere, and was due almost entirely to near-zero static stability. This most likely arose as a result of cooling via longwave flux divergence below CDO top. The third type of turbulent layer existed well outside the CDO and was produced by large local vertical wind shear. The shear maxima associated with the beneath-cloud and outside-CDO turbulent layers produced a sharp transition from weak inflow below to strong outflow above. The results suggest the CDO creates its own distinctive stability profile that strongly influences the distribution of turbulence and the transition to outflow in tropical cyclones.

1. Introduction

The horizontally extended, long-lasting “central dense overcast” (CDO) found within the outflow layer of mature tropical cyclones represents one of the most dramatic cirrus cloud layers in the subtropics. The CDO can be as much as 400 hPa thick near the storm center. Cirrus cloud tops lie at the elevated tropopause within the eyewall region and descend outward from the storm center in an umbrella shape (Cairo et al. 2008). Outside the storm core, a "moat" exists in which convection is largely inactive (e.g., Molinari et al. 1999). In this region the cirrus deck thins with increasing radius but still covers most of the circulation. Outside about the 200 km radius, renewed deep convection is widespread within outer bands. Continuous cirrus cloud cover often is present out to or beyond the 300 km radius, with thin and likely also subvisible cirrus (e.g., Dinh et al. 2010) extending considerably farther. Distinct bands are often observed in cirrus, both within and on the edge of the CDO. Knox et al. (2010) have shown that such cirrus bands occur not just in tropical cyclones, but in turbulence near mesoscale convective systems (MCSs) and on the anticyclonic shear side of midlatitude jets.

Trier and Sharman (2009) and Trier et al. (2010) used observations and high-resolution numerical simulations to investigate turbulence within cirrus bands north of an MCS. Vertical wind shear played two roles: it directly reduced Richardson number (*Ri*), and it created differential horizontal advection of θ_e that reversed the sign of $\partial\theta_e/\partial z$ and thus created a (moist) *Ri* less than zero at the outer part of the cirrus anvil. The bands took the form of shallow convective roll vortices like those seen in the planetary boundary layer. These rolls became strong only in the presence of cloud-radiative interaction in their simulations, suggesting that radiative processes within the anvil played an important role.

The tropical cyclone CDO represents a larger and deeper cirrus layer that has the potential to contain the same turbulent processes as the MCS. Longwave warming exists at the base of the CDO and longwave cooling in the upper part (Fovell et al. 2009; Bu et al. 2014; Melhauser and Zhang 2014). These radiative processes have the potential to contribute to small static stability in the upper troposphere. In addition, outflow jets are frequently present that contain strong vertical wind shear at their base (e.g., Merrill and Velden 1996). The ingredients are thus present for low Richardson number and potential turbulence. Consistent with this view, Emanuel and Rotunno (2011) produced a revised closure for their theory of tropical cyclones that explicitly assumed *Ri* in the outflow layer remained near its critical value for turbulence. This condition played an essential role in connecting the dynamics of the storm core to that of the outflow layer. Despite the potential importance of turbulent processes, almost no measurements of *Ri* in tropical cyclones have been made, and the influence of the CDO on tropical cyclone dynamics and thermodynamics has not been investigated.

This study makes use of dropsondes released from the upper troposphere in tropical cyclones. They reveal the frequent existence of turbulent layers within, beneath, and outside the CDO. The structure and causes of these layers, and their relationship to processes within tropical cyclone outflow, are described.

2. Data and Methods

Data for this study come from GPS sondes (Hock and Franklin 1999) that were released within 1000 km of the center of tropical cyclones by the NOAA G-IV aircraft over 7 years (1997-1999; 2002-2005). The sondes in this study were the same as those used by Molinari et al. (2012), except that about 100 additional sondes were included here because small gaps in dew point were accepted that were not allowed in the earlier CAPE calculations. The data were

interpolated to 100-m vertical spacing. Linear interpolation in temperature, dew point, and wind was performed across less than 400 m gaps in the soundings. No supplementation of the sondes above the release point from global model gridded analyses was carried out in this study. After this processing, 2571 sondes remained for analysis.

The G-IV sondes have a mean release elevation near 13 km (175 hPa). Molinari et al. (2012) showed a fairly uniform distribution of sondes with respect to radius and azimuth within 1000 km of the center. The sondes are not released on a uniform grid, but rather might represent only certain quadrants and radial ranges in any given flight. Composite analyses will be carried out by averaging these irregularly-spaced sondes in 100-km radial bins. A radius-height (r-z) section of the number of sonde observations in each 100-km radial bin (color shading) is shown in Fig. 1. The number peaks at radii between 300 and 600 km and below the 12-km elevation. Only 27 sondes were available between the storm center and the 100 km radius. That region will not be addressed.

Fig. 1 also shows the radial-vertical distribution (contoured) of the number of sonde observations in Hurricane Ivan (2004). More than 320 sondes were deployed, the most of any individual storm in this study. They covered the period 9-16 September, as the storm moved from near 10°N, 50°W to the central Gulf of Mexico. Later sections of the paper will focus solely on Hurricane Ivan. Only those levels and radius bins with 10 or more observations will be included in the analyses. For all but 12 hours of the sonde collection, Ivan was a major hurricane with maximum winds exceeding 110 kt (57 m s^{-1}). The history of Hurricane Ivan is described in the National Hurricane Center (NHC) report of the storm (http://www.nhc.noaa.gov/pdf/TCR-AL092004_Ivan.pdf).

Because dropsonde data are available only at discrete levels in the vertical, a bulk Richardson number (R_B) is utilized. The critical value for turbulence is lost in this discretization, making an empirical estimate of the criterion for turbulence somewhat larger than 0.25 (e.g., Stull 1998). Nevertheless, if $R_B \leq 0.25$ in a discrete layer, turbulence is almost certain to exist somewhere within the layer. When R_B exceeds 0.25 but is less than unity, turbulence might or might not be present (e.g., Lane et al. 2012). For simplicity in this paper, $0.25 < R_B < 1$ will be labeled a "low Richardson number layer" and $R_B \leq 0.25$ a "turbulent layer". R_B will be calculated over 400 m layers every 100 m in the vertical. R_B is given by:

$$R_B = \frac{\frac{g}{\overline{\theta_v}} \frac{\Delta \theta_v}{\Delta z}}{\frac{(\Delta u)^2 + (\Delta v)^2}{(\Delta z)^2}} \qquad (1)$$

where Δz is 400 m, other differences are between the top and bottom of the layer, θ_v is virtual potential temperature, and the bar indicates a mean over the layer. No Richardson number was calculated within any layers of missing data greater than 400 m. The only exception was for missing relative humidity above the 9-km level, for which a value of 50% was assumed. This will have little impact on R_B calculations owing to the small saturation vapor pressure at those high levels. Storm-relative winds (i.e., with tropical cyclone motion subtracted) were used in (1), but measured winds give the same result because the storm motion has no vertical derivative. The numerator (stability) and denominator (shear squared) of Eq. 1 will sometimes be displayed separately and expressed in units of 10^{-4} s^{-2}.

For saturated layers it is appropriate to calculate a moist Brunt-Väisälä frequency (Durran and Klemp 1982; Trier et al. 2010). Trier et al. (2010) calculated a full moist Richardson number, but this was done from numerical model output, for which all variables, including liquid

and ice mixing ratios, were known at every point. Dropsondes contain numerous limitations that make such a calculation problematical. These include: (i) a dry bias that sometimes does not produce saturation even in cloudy layers (Jaubert et al. 1999); (ii) missing dew points in the upper troposphere due to instrument limitations at low temperatures; and (iii) no estimates for condensate mixing ratios. The first two limitations made it difficult to even identify saturated layers. For instance, the Appendix shows that almost *no* saturated layers existed in the Hurricane Ivan dropsonde data either below 4 km or above 12 km (the latter often due to missing dew points). This is not realistic in a major hurricane.

The Appendix shows that the moist Brunt-Väisälä frequency in the R_B calculation produced differing results from the dry estimates within saturated layers in the low and middle troposphere. Nevertheless, it is argued that the results of this paper are largely unaffected by the use of the dry R_B from Eq. 1. Three major types of low Richardson number will be identified: the first occurred in clearly unsaturated layers beneath cirrus; the second high in the troposphere where the dry and moist estimates approach one another; and the third in the upper troposphere well outside the storm core where the air was usually clear. In none of those examples was the moist Richardson number critical. Equally important, identifying saturated layers with the dropsondes was difficult as noted above. For all of these reasons, following Kudo (2013) and Luce et al. (2010), only dry Richardson number estimates were considered in the body of the paper. The Appendix provides a more detailed discussion of these issues.

The thickness of the layer used in Eq. 1 was chosen to be equal to the largest data gap over which interpolation was carried out. Typical dropsonde errors of 0.2°C and 0.5-2.0 m s^{-1} (Hock and Franklin 1999) could produce large errors in R_B over such a narrow layer. However, such measurement errors are likely correlated in the vertical, and this would reduce errors in vertical

gradients. Conservative decisions were made with regard to vertical spacing: 100 m is considerably coarser than the raw sounding resolution, and R_B was calculated over 400 m rather than 100 m. The results will be presented primarily in terms of the percentage of sondes for which R_B falls below a particular value. Evidence will be presented in the following section that errors in these percentages are much smaller than the signal.

In order to distinguish R_B distribution within tropical cyclones from that in the typical hurricane season subtropical environment, R_B was also computed from high-resolution rawinsonde data available from State University of New York/Stony Brook (http://www.sparc.sunysb.edu/). Four sets of twice-daily subtropical rawinsondes during the months of August and September were chosen from Miami and San Juan (each 1998-2008), Seawall Airport in Barbados (1998-2003), and Grand Cayman (1998-2001). Any rawinsonde at these four locations that fell within 1000 km of the center of a tropical cyclone at the sonde release time was removed. The resultant data from the four sets of subtropical rawinsondes will be labeled the "non-tropical cyclone rawinsondes" to distinguish them from the G-IV sondes, all of which were within 1000 km of a tropical cyclone. The non-tropical cyclone data is made up of 2466 sondes, comparable in number to that from the G-IV.

Finally, 96 rawinsondes from the Stony Brook data between 1998 and 2011 that were within 500 km of a major hurricane were examined. Although their number is small, these sondes provide confirmation of the maximum in turbulence at the upper limit of G-IV sonde data in Hurricane Ivan.

3. Results

a. G-IV sondes

The potential for small R_B in the upper troposphere of tropical cyclones becomes apparent in Fig 2, which shows R_B and its individual components, averaged over all G-IV sondes. Stability is fairly large above the boundary layer, but small from 10-13 km elevation. This reflects the combined influence of the warm core in the upper troposphere, in which isentropes turn downward, and the cold core at the tropopause where the isentropes turn upward. Vertical shear increases upward from the midtroposphere. This combination produces a second region in tropical cyclones of small R_B (along with the planetary boundary layer) in which turbulence might be common. Part of the goal of this paper is to evaluate the role of CDO physics and dynamics in producing this structure.

The fraction of sondes with low R_B provides another means of assessing the opportunity for turbulence. Fig. 3 shows this fraction for three sets of data: G-IV sondes in depressions, storms, and Category 1 and 2 hurricanes (blue); G-IV sondes from major (Category 3-5) hurricanes (red); and non-tropical cyclone rawinsondes (black). The maximum in the frequency of $R_B < 1$ (Fig. 3a) occurred in the planetary boundary layer, as expected. A minimum in low R_B frequency was present from 1.5-7 km. Each dataset showed an increase of frequency with height above the middle troposphere to a prominent secondary maximum in the upper troposphere. The weak and strong tropical cyclones deviated from the non-tropical cyclone background above 8 km. Maximum upper tropospheric low R_B fraction in tropical cyclones reached 45-55% near 13 km, which represents the top level that is sufficiently represented by the dropsondes. The fraction of sondes meeting the turbulence criterion (Fig. 3b) also indicates an increase in the upper troposphere, peaking at 20% just above the 13 km level for major hurricanes. Overall, 96% of G-IV sondes contained at least one layer with $R_B < 1$ and 35% with $R_B \leq 0.25$ above z = 7.5 km.

One concern in Fig. 3 is the high percentage of low R_B appearing near the upper limit of G-IV sonde availability (Fig. 1). To confirm these results, the same calculations were made from all *rawinsondes* within 500 km of the center of tropical cyclones (Fig. 4). This figure gives virtually the same levels of peak low R_B frequency just above the 13-km level. Percentages of turbulence and of low R_B decrease above that level to minimum values near 17 km. The vertical structure of the low R_B region coincides with the CDO layer shown for a single storm by Cairo et al. (2008), implying that the CDO might play a role in the turbulence.

The layers between 2 and 7 km elevation contain relatively high stability and small vertical wind shear (Fig. 2) and thus should not exhibit frequent instances of low R_B. In those layers only about 5% of sondes met the low R_B criterion, and 1.5% met the turbulence criterion (Fig. 3a,b). Even if sonde measurement errors were responsible for *every* one of these low Richardson numbers between 2 and 7 km, it would imply an error rate much smaller than the substantial maxima in the boundary layer and outflow layer. It appears that any possible measurement errors did not contribute meaningfully to the distribution of low R_B and turbulent layers found in this study.

The turbulence criterion was met in 44% of sondes in major Hurricane Ivan over at least one layer above 7.5 km height. The remainder of this paper will examine Hurricane Ivan sondes in detail in order to understand the physical mechanisms that produced these turbulent layers.

b. Turbulent layers in Hurricane Ivan

An r-z section of storm-relative radial velocity in Fig. 5 shows outflow reaching a maximum near the 12-km level. Large vertical shear of the radial flow existed at middle radii at 9-11 km height, and at outer radii at 11-12 km height.

The CDO structure can be seen in the mean relative humidity in Fig. 6. Relative humidity peaked at 10.5 – 11.5 km elevation, with high values extending outward to middle radii of the storm. The percentage of sondes with low R_B and with the turbulence condition met are also plotted. Low R_B exceeded 15% over the entire outflow layer. The peak frequency of low R_B was found in two locations: the upper troposphere at small radii, just above the core of the CDO; and at 900-1000 km radii, well outside the CDO. The frequency of turbulent layers peaked in the same regions. Both R_B criteria show secondary maxima at middle radii near the outer edge of the CDO.

The structure of turbulent layers in Hurricane Ivan was investigated for each individual sonde. Three prominent signatures arose. The first emerged only *below* cirrus base and resulted almost entirely from low stability. This signature appeared in at least one 400-m layer in 16% of dropsondes. The second appeared only *above* cirrus cloud base (32% of sondes), and again was associated primarily with low static stability. The third signature of turbulence arose mostly in clear air outside the CDO at larger radii (3% of sondes) and resulted primarily from large vertical wind shear. The low percentage of the last type of turbulent layer arose in part because fewer G-IV sondes were released at large radii (see Fig. 2 from Molinari et al. 2012).

Composites were constructed for each type of turbulent layer. Members of these composites were chosen subjectively that provided a subset of clean examples. Thus, for instance, if multiple turbulent layers with differing structure appeared in a single sounding, that sounding was not included in a composite.

i. Below-cloud turbulent layers

The first prominent signature of $R_B \leq 0.25$ in the Hurricane Ivan sondes existed below cloud base and occurred in 16% of sondes. Two identifiable subgroups were isolated. The first,

with 12 sondes, displayed the precipitation sublimation signature described by Luce et al. (2010) and Kudo (2013), which includes a vertical wind shear maximum above cloud base. The second group (13 sondes) was qualitatively identical to the first beneath cloud base, but displayed no shear maximum just above. Because both groups were similar other than the local difference in wind shear, only the 12-sonde composite will be shown.

Two examples of below-cloud turbulent layers are shown in Fig. 7. The top panels show each of the sonde locations plotted on an infrared satellite image closest to sonde release time. The remaining panels show R_B and its components and a Skew T-log p plot for each sounding. The magenta bar indicates the 400-m thick turbulent layer.

Both sondes shown in Fig. 7 were released within the CDO at radii of 329 and 534 km, respectively. The Skew T-log p diagrams show that cloud base was located just below 300 and 350 hPa, respectively, in the layer where the relative humidity fell from saturation (with respect to ice) to very low values below. In both soundings a distinct stable layer coincided with cloud base. Just above this layer, vertical shear exhibited narrow maxima of 22 and 19 m s^{-1} km^{-1}, respectively. This corresponded to a turning of the wind, especially in Fig. 7d, where cyclonic inflow turned to strong outflow. Beneath the stable layer, and thus beneath cloud base, static stability became slightly negative. The turbulent layers coincided with this low stability.

A composite of the 12 soundings that displayed similar structure are shown in Fig. 8. Relative humidity, stability, radial and tangential wind components, and R_B are displayed in the four panels. The cyan shading represents the cloud layer. The composite turbulent layer was located at a height of 9.3 km and a radius of 491 km, near the outer edge of cirrus clouds in the storm.

Relative humidity (Fig. 8a) exceeded 95% over the lowest km of the cloud, then fell sharply to less than 35% beneath the cloud, a surprisingly low value in the vicinity of a tropical cyclone. The large stability variations revealed in the individual soundings also emerged in the composite. Maximum stability (Fig. 8b) was found in the lowest 100 m of the cloud and minimum stability 500 m below cloud base. Weak inflow and cyclonic flow (Fig. 8c) existed in the midtroposphere through the top of the turbulent layer. Just above, at the level of the stable layer, a sharp transition to strong outflow was present. The value of R_B remained above 2 through most of the troposphere and fell to near unity in the upper troposphere (Fig. 8d). The turbulence criterion was met only beneath cloud base.

The stability and shear variations shown in Figs. 7-8 closely resembled those produced by sublimation of precipitation shown by Luce et al. (2010) and Kudo (2013). A schematic diagram for these turbulent layers is given in Fig. 9. When precipitation falls from cirrus into dry air, it quickly sublimates and produces a cold anomaly. If sublimation is strong enough, a strong stable layer develops above this cold anomaly (thus at and just above cloud base) and a statically unstable or near-neutral layer develops beneath it. The critical R_B for turbulence in the composite arose almost entirely due to the negative stability anomaly; vertical wind shear was modest or small in these layers.

The composite structure in Fig. 8 displayed strong vertical wind shear (exceeding 20 m s^{-1} km^{-1}) immediately above the stable layer. The composite wind direction changed by 50° in a single 400-m layer as the radial velocity in the storm sharply veered from inflow to outflow (Fig. 8c). In tropical cyclone numerical simulations, vertically propagating gravity waves are extremely common within 200 km of convection (Fuqing Zhang, personal communication, 2013). It is speculated that the ducting or partial ducting of gravity waves by the stable layer

could produce such a shear maximum (e.g., Hooke 1986). Alternatively, mixing in the unstable layer below could reduce the vertical shear, creating an increase in shear in the layer immediately above. Regardless of the cause, the combination of shear and stability fluctuations associated with sublimation appeared to play a direct role in determining the base of the outflow layer in these sondes.

ii. Low stability within the CDO

Nearly one third of Hurricane Ivan sondes displayed upper tropospheric turbulent layers in the presence of cirrus clouds. The two sondes shown in Fig. 10 were released at r = 176 and 204 km, respectively, closer to the center than most sondes in the beneath-cloud turbulent layers in Figs. 7-8. The first sonde was released in a region with a cloud top temperature of about -44°C (Fig. 10a), whereas the sounding indicates the low R_B layer lies at about -55°C (Fig. 10c). This suggests the unstable layer lies above cloud top. But if the clouds were partly transparent to IR radiation, as is common with thin cirrus, the brightness temperature might be overestimated and thus the cloud top height underestimated. It cannot be said with any certainty that the low R_B layer was within or above cloud.

The second sonde in Fig. 10 was located where the infrared cloud top temperature was -70°C. The turbulent layer within this sounding (Fig. 10d) was centered at -54°C. As a result, the turbulence in the second sounding lies unambiguously within the cloud layer. Both turbulent layers were found in regions with tropospheric-deep clouds.

A composite of 30 such cases was created that was restricted to turbulent layers located above the 12-km level. The mean radius of these sondes was 358 km, and all were released at a location with clear visual evidence for cirrus clouds on infrared satellite images. About two thirds of sondes in this composite displayed tropopospheric-deep cloud as in Fig. 10, while the

remainder had subsaturated middle levels. Composite relative humidity (Fig. 11a) indicates a cloud base near the 11-km level. The turbulent layer existed well above cloud base, where composite relative humidity fell to about 60%. It is uncertain whether this subsaturated value still fell within the cloud layer. Garrett et al (2005) noted that thin cirrus can exist with humidity near 60% and still have a significant radiative impact. It is also possible that the drop in relative humidity values aloft arose due to the reduced frequency of dew point observations at this high level (dashed line segment in Fig. 11a). Given the small mean radius of this composite and the typical top of the CDO well above the 13 km level (Cairo et al. 2008), it is hypothesized that the composite turbulent layer in Fig. 11 lies within cloud.

Consistent with the soundings in Fig. 10, the composite turbulent layer resulted almost entirely from a strong decrease in stability (Fig. 11b,d). In contrast to the beneath-cloud composite, the turbulent layer existed well above the base of the outflow layer (Fig. 11c). The tangential velocity showed deep cyclonic flow for the entire layer up to the 13 km level. This reflects in part the small mean radius for this composite, closer to the center than the first composite.

Given the complexity of longwave radiative fluxes in cirrus clouds, which depend not only on cloud thickness, but also on particle size and density (e.g., Ackerman et al. 1988), the cause of the turbulent layer shown in Fig. 11 could not be determined with certainty. Longwave flux divergence and cooling beneath cloud top and longwave warming within the cloud (Bu et al. 2014; Melhauser and Zhang 2014) would contribute to this stability anomaly, and it appears likely that these processes are playing a role. Regardless of the cause, it was striking that one third of sondes in Hurricane Ivan exhibited evidence for turbulence at a level above cirrus base.

iii. Shear-induced turbulent layers

Two examples of turbulent layers produced by large vertical wind shear are displayed in Fig. 12. These sondes were released at r = 836 km (Fig. 8a) and 537 km (Fig. 8b). Turbulence was associated primarily with a maximum in vertical wind shear within a transition from weak cyclonic flow to strong anticyclonic outflow.

A composite of 11 sondes with shear-induced turbulent layers in Hurricane Ivan (Fig. 13) was constructed by requiring both $R_B \leq 0.25$ and the shear term in Eq 1 exceeding 2 X 10^{-4} s^{-2} (14 m s^{-1} km^{-1}). These turbulent layers fell generally outside the CDO at a mean radius of 837 km. The general lack of cloudiness in these profiles showed in relative humidity below 50% at all levels above 3 km (Fig. 13a). The composite wind shift within the turbulent layer (not shown) amounted to almost 60° over 400 m. R_B was large through the lower and middle troposphere (Fig. 13d), and fell below unity only in the turbulent layer. This turbulence composite reveals a sharp transition to the outflow layer (Fig. 13c) that is not directly associated with cloud-induced diabatic effects.

4. Discussion

Dropsondes from the NOAA G-IV aircraft were used to examine the presence of low bulk Richardson number (R_B) in tropical cyclones. Above the planetary boundary layer the maximum frequency of $R_B < 1$ ("low R_B") and $R_B \leq 0.25$ ("turbulence") was located in the upper troposphere. The fraction of sondes with low R_B exceeded 50% just above the 13-km level in major hurricanes. The non-tropical cyclone environment exhibited a maximum of only 25% at levels near 11.5 km. Turbulence reached a maximum frequency above the 12-km level of 10% in weaker tropical cyclones and 20% in major hurricanes, several times more frequent than outside of tropical cyclones. Major Hurricane Ivan (2004) was studied in detail.

Three predominant prototypes of turbulent layers were shown in Hurricane Ivan: beneath cloud base near the edge of the CDO (16% of sondes); well above cloud base within the CDO (32% of sondes); and at the base of the outflow layer outside the CDO (3% of sondes). Overall, 44% of sondes exhibited $R_B \leq 0.25$ in at least one upper tropospheric layer (the sum of the previous numbers exceeded 44% because some sondes exhibited multiple types of low R_B). Each of these turbulence types will be discussed in detail below.

a. Turbulence associated with the sublimation of precipitation

The turbulent layers in this composite were located beneath the base of the CDO, at a mean radius of 491 km and a mean height of 9.3 km. They were found near the outer edge of the CDO, but only in the presence of relative humidity below 40%. The schematic in Fig. 9 resembles the structure induced by sublimation of frozen precipitation shown by Luce et al. (2010) and Kudo (2013). The extreme dryness of the layers would enhance the sublimation rate and make unstable lapse rates more likely (Schultz et al. 2006). This type of turbulent signature was rarely found near the storm core in this study because soundings were too moist.

The satellite image shown by Kudo (2013; his Fig. 2) indicated that the turbulent layers were located within the extended CDO of a typhoon, but likely one that was undergoing extratropical transition. Kudo's sounding and flight-level data indicated a relatively low cloud base near 500 hPa. The well-mixed turbulent layer was present between 505 and 610 hPa, over a temperature range of 0°C to -15°C. These layers were well beneath those shown in the below-cloud turbulence composite in this study, and at higher temperature. A search of the Hurricane Ivan data turned up 13 soundings that exhibited turbulent layers at levels and at temperatures comparable to Kudo (2013).

On the basis of his simulations, Kudo argued that, other things being equal, turbulence will be weaker at colder temperatures. In particular, vertical velocity oscillations were half the magnitude when the stable layer temperature was -20°C versus -10°C. In contrast, the beneath-cloud turbulence composite in this study exhibited a mean cloud-base temperature of -28.5°C, not unlike that observed by Luce et al. (2010). The reason for the lack of turbulence at these temperatures in the simulations of Kudo (2013) is uncertain. It is possible that larger precipitation rates or more continuous precipitation are needed at lower temperatures. The results here suggest that upper tropospheric, sublimation-induced turbulence at temperatures below -25°C were about three times more common than the warmer midtropospheric examples in the one major hurricane that was studied in detail.

Kudo's (2013) study was prompted by turbulence observations from aircraft. Pilot reports and eddy dissipation rate data from commercial aircraft provide a direct measure of turbulence location and magnitude. Work is underway to evaluate this reported turbulence in the vicinity of tropical cyclones, and to determine the variation of Richardson number in nearby rawinsondes.

b. Turbulence above cirrus base

The second type of turbulent layer in Hurricane Ivan appeared in 32% of dropsondes. The 30-sonde composite was found at a mean radius of 358 km, close to the storm center rather than near the edge of the CDO. Turbulence existed 2.5 km above cloud base (Figs. 10-11) and thus was likely influenced by diabatic processes within the CDO. As with sublimation-induced turbulence, it arose almost entirely from low stability. Bu et al. (2014) and Melhauser and Zhang (2014) have noted the negative vertical gradient in longwave heating from cirrus base to cirrus top. This has the potential to create unstable lapse rates within the cloud layer. Garrett et al. (2005) attributed cloud-top cooling within the anvil of a thunderstorm to shielding of the cloud

top from surface upwelling radiation. However, Garrett et al. (2005) did not find *Ri* values indicative of turbulence in the anvil. The question arises as to why such events were so common in Hurricane Ivan studied in this paper. Because more than 2/3 of members of this composite displayed deep saturated or nearly saturated layers beneath the turbulent layer (see examples in Fig. 10), it is hypothesized that the thickness of the CDO near the tropical cyclone center enhanced the shielding effect and thus the cloud-top cooling, making low stability and turbulence more likely.

Cloud-top cooling is accompanied by shortwave warming during the day. The G-IV sondes in this study were primarily released late afternoon/early evening local time, with a second subset during overnight hours. Virtually none were released when the sun was high in the sky. Recent results by Melhauser and Zhang (2014; their Fig. 9) suggest that shortwave warming destabilizes the upper troposphere within the cirrus overcast even more strongly than longwave radiative processes. Sondes released by the NASA Global Hawk (Braun et al. 2013) show promise in further understanding the role of cirrus layer warming and cloud-top cooling, because they cover a wider range of the diurnal cycle and are released above the CDO top. Despite the uncertainty surrounding the mechanism, the presence of upper tropospheric turbulence in nearly one third of sondes in Hurricane Ivan makes this a worthy topic for further study.

c. Turbulence outside the CDO

The third type of turbulent layer arose almost entirely from exceptional vertical wind shear at the base of the outflow layer. It was found at a mean elevation of 11.5 km and a mean radius of 837 km, well outside the edge of the CDO. The vertical shear maximum separated layers of differing origin: strong anticyclonic outflow from the storm core was present above the turbulent layer, and weak cyclonic inflow below (Figs. 12-13). Tropical cyclones exhibit substantial

inward fluxes of angular momentum by azimuthal eddies (Pfeffer and Challa 1981; Molinari and Vollaro 1989) that maximize at larger radii. They drive mean outflow where such fluxes increase upward, and inflow below and above (Holland and Merrill, 1984; Molinari and Vollaro 1989). The eddy momentum source within outflow jets thus helps to produce mean upper tropospheric inflow beneath the outflow jets that contribute to the sharpness of the outflow layer, and potentially to turbulence at the base of the outflow.

d. Other causes of turbulence

The results provide strong evidence that the CDO organizes its own stability field via diabatic effects. The two CDO-based turbulent layers (both below and above cloud base) exhibited low stability associated with the impacts of latent and/or radiative heating and cooling. The third turbulent layer was characterized almost entirely by large shear. However, many turbulent layers were found with both negative stability anomalies and positive shear anomalies. Gravity waves produce alternating layers of stability and shear anomalies, and as a result, high and low Richardson number (e.g., Lane et al. 2012; Fovell et al. 2007). It is possible that gravity waves are responsible for some of the turbulent layers not included in the three composites. Subsequent study will examine the role of gravity waves in the structure of the outflow layer.

This paper focused on layers with $R_B \leq 0.25$, but in three-dimensional flows with both horizontal and vertical shears, turbulence can occur when $R_B < 1$ (Knox et al. 2010; Lane et al. 2012). In particular, a correspondence has been found between regions of negative absolute vorticity (and thus inertial instability) and turbulence (Dunkerton 1981; Knox et al. 2010). Low inertial stability is known to exist in tropical cyclone outflow (Rappin et al. 2011). The relationships in tropical cyclones among diabatic physics, turbulence, gravity waves, and inertial and symmetric instability represent a promising area of future research.

Acknowledgements. We thank Dr. Brian Tang of our department for helpful discussions of this work. NOAA G-IV dropsonde data were obtained from the Hurricane Research Division of NOAA. High-resolution rawinsonde data were obtained from the SPARC Data Center at the State University of New York/Stony Brook (http://www.sparc.sunysb.edu/). This paper was supported by NSF grants ATM0855718 and AGS1132576 and NASA grant NNX12AJ81G.

APPENDIX: INFLUENCE OF USING A MOIST BRUNT-VÄISÄLÄ FREQUENCY

The results shown in the body of the paper made use of a dry Brunt-Väisälä frequency, even in saturated regions. In such regions, Durran and Klemp (1982) noted that the dry estimates did not correctly represent the stability term within the Richardson number. They provided an accurate estimate for the Brunt-Väisälä frequency in saturated layers:

$$N_m^2 = g(ab - c) \qquad \textbf{(A1)}$$

where

$$a = \frac{1 + \dfrac{Lq_s}{RT}}{1 + \dfrac{\varepsilon L^2 q_s}{c_p R T^2}}, \qquad \textbf{(A2)}$$

$$b = \frac{1}{\theta}\frac{d\theta}{dz} + \frac{L}{c_p T}\frac{dq_s}{dz}, \qquad \textbf{(A3)}$$

$$c = \frac{d(q_\ell + q_s)}{dz}, \qquad \textbf{(A4)}$$

q_ℓ is the liquid water mixing ratio, and $\epsilon = 0.622$. In this appendix, the challenges of using (A1) with dropsonde data are noted, and arguments are made that the dry estimates retained considerable value for the types of turbulent layers studied in this paper. The liquid water mixing ratio was omitted in Eq. (A4) because it was unknown from the dropsonde data.

Saturation rarely existed in the sonde data. Only RD93 sondes from Vaisala were used in this study, and these have a known dry bias (e.g., Jaubert et al. 1999). In addition to this sensor issue, dropouts of dew point temperature were fairly common at low temperatures in the upper troposphere. Fig. A1 shows the number of sondes that exhibited saturation or supersaturation as a function of height for Hurricane Ivan and for the entire G-IV data set. Many levels in Hurricane

Ivan contained fewer than 5 observations of saturation. Fewer than 1% of the G-IV sondes exhibited saturation in the middle troposphere and above 12 km. The frequency of saturation was not well represented in these layers.

Richardson number was calculated using Eq. (A1) for all available saturated layers in the G-IV data set. The fraction of $R_B < 0.25$ in these layers is shown in Fig. A2. For comparison, the same results from the dry calculation (equivalent to the sum of the red and blue lines in Fig. 3b) are also displayed. Fig. A2 shows that the frequency of $R_B < 0.25$ in saturated layers was much larger in the lower and middle troposphere than shown by the dry calculation. The high fraction of moist turbulent layers below 4 km is a topic worthy of further study, but the lack of a true estimate of saturation in these layers noted above does not allow such a study to be carried out with the available data.

The limited results shown in Fig. A2 leave no doubt, consistent with Durran and Klemp (1982), that a moist Richardson number must be used in saturated layers. Nevertheless, it is argued that the dry R_B calculations shown in the body of the paper were largely uninfluenced by these results, because turbulent layers existed (i) in clearly unsaturated layers beneath cirrus (Figs. 7-8); (ii) high in the troposphere where the dry and moist estimates approach one another (Figs. 10-11); and (iii) well outside the storm core where the air was usually clear (Fig. 13). In none of those examples was the moist Richardson number critical.

REFERENCES

Ackerman, T.P., K.-N. Liou, F.P.J. Valero, and L. Pfister, 1988: Heating rates in tropical anvils. *J. Atmos. Sci.*, **45**, 1606-1623.

Braun, S.A., R. Kakar, E. Zipser, G. Heymsfield, C. Albers, S. Brown, S.L. Durden, S. Guimond, J. Halverson, A. Heymsfield, S. Ismail, B. Lambrigstsen, T. Miller, S. Tanelli, J. Thomas, and J. Zawislak, 2013: NASA's genesis and rapid intensification processes (GRIP) field experiment. *Bull. Amer. Meteor. Soc.*, **94**, 345-363.

Bu, Y.P., R. Fovell, and K.L. Corbosiero, 2014: Influence of cloud-radiative forcing on tropical cyclone structure. *J. Atmos. Sci.*, 1644-1662.

Cairo, F., C. Buontempo, A.R. MacKenzie, C. Schiller, C.M. Volk, A. Adriani, V. Mitev, R. Matthey, G. DiDonfrancesco, A. Oulanovksy, F. Ravegnani, V. Yushkov, M. Snels, C. Cagnazzo, and L. Stefanutti, 2008: Morphology of the tropopause layer and lower stratosphere above a tropical cyclone: a case study on cyclone Davina (1999). *Atmos. Chem. Phys.*, **10**, 3411-3426.

Dinh, T.P., D.R. Durran, and T.P. Ackerman, 2010: Maintenance of tropical tropopause layer cirrus. *J. Geophys. Res.*, **115**, D02104.

Dunkerton, T.J., 1981: A nonsymmetric equatorial inertial instability. *J. Atmos. Sci.*, **40**, 807-813.

Durran, D.R., and J.B. Klemp, 1982: On the effects of moisture on the Brunt-Väisälä frequency. *J. Atmos. Sci.*, **39**, 2152-2158.

Emanuel, K.A., and R. Rotunno, 2011: Self-stratification of tropical cyclone outflow. Part I: Implications for storm structure. *J. Atmos. Sci.*, **68**, 2236-2249.

Fovell, R.G., R.D. Sharman, and S.B. Trier, 2007: A case study of convectively-induced clear-air turbulence. *12th Conf. on Mesoscale Processes*, Waterville Valley, NH, Amer. Meteor. Soc., 13.4 [Available online at http://ams.confex.com/ams/pdfpapers/126190.pdf].

Fovell, R.G., K.L. Corbosiero, and H.-C. Kuo, 2009: Cloud microphysics impact on hurricane track as revealed in idealized experiments. *J. Atmos. Sci.*, **66**, 1764-1778.

Garrett, T.J., B.C. Navarro, C.H. Twohy, E.J. Jensen, D.G. Baumgardner, P.T. Bui, H. Gerber, R.L. Herman, A.J. Heymsfield, P. Lawson, P. Minniss, L. Nguyen, M. Poellot, S.K. Pope, F.P.J. Valero, and E. M. Weinstock, 2005: Evolution of a Florida cirrus anvil. *J. Atmos. Sci.*, **62**, 2352-2372.

Hock, T.F., and J.L. Franklin, 1999: The NCAR GPS Dropsonde. *Bull. Amer. Meteor. Soc.*, **80**, 407-420.

Holland, G.J., and R.T. Merrill, 1984: On the dynamics of tropical cyclone structural changes. *Quart. J. Roy. Meteor. Soc.*, **110**, 723-745.

Hooke, W.H., 1986: Gravity waves. In *Mesoscale Meteorology and Forecasting*, Ed. P.S. Ray, Amer. Meteor. Soc., 272-288.

Jaubert, G., C. Piriou, S.M. Loehrer, A. Petitpa, and J.A. Moore, 1999: Development and quality control of the FASTEX data archive. *Quart. J. Roy. Meteor. Soc.*, **125**, 3165-3188.

Knox, J.A., A.S. Bachmeier, W.M. Carter, J.E. Tarantino, L.C. Paulik, E.N. Wilson, G.S. Bechdol, and M.J. Mays, 2010: Transverse cirrus bands in weather systems: a grand tour of an enduring enigma. *Weather*, **65**, 35-41.

Kudo, A., 2013: The generation of turbulence below midlevel cloud bases: The effect of cooling due to sublimation of snow. *J. Appl. Meteor. and Clim.*, **52**, 819-833.

Lane, T.P., R.D. Sharman, S.B. Trier, R.G. Fovell, and J.K. Williams, 2012: Recent advances in the understanding of near-cloud turbulence. *Bull. Amer. Meteor. Soc.*, **93**, 499-516.

Luce, H., T. Nakamura, M.K. Yamamoto, M. Yamamoto, and S. Fukao, 2010: MU radar and lidar observations of clear-air turbulence underneath cirrus. *Mon. Wea. Rev.*, **138**, 438-452.

Melhauser, C., and F. Zhang, 2014: Diurnal radiation cycle impact on the pregenesis environment of Hurricane Karl (2010). *J. Atmos. Sci.*, **71**, 1241-1259.

Merrill, R.T., and C.S. Velden, 1996: A three-dimensional analysis of the outflow layer of Supertyphoon Flo (1990). *Mon. Wea. Rev.*, **124**, 47-63.

Molinari, J., and D. Vollaro, 1989: External influences on hurricane intensity: Part I. Outflow layer eddy angular momentum fluxes. *J. Atmos. Sci.*, **46**, 1093-1105.

Molinari, J., P. Moore, and V. Idone, 1999: Convective structure of hurricanes as revealed by lightning locations. *Mon. Wea. Rev.*, **127**, 520-534.

Molinari, J., D.M. Romps, D. Vollaro, and L. Nguyen, 2012: CAPE in tropical cyclones. *J. Atmos. Sci.*, **69**, 2452-2463.

Pfeffer, R.L., and M. Challa, 1981: A numerical study of the role of eddy fluxes of momentum in the development of Atlantic hurricanes. *J. Atmos. Sci.*, **38**, 2393-2398.

Rappin, E.D., M.C. Morgan, and G.J. Tripoli, 2011: The impact of outflow environment on tropical cyclone intensification and structure. *J. Atmos. Sci.*, **68**, 177-194.

Schultz, D.M., K.M. Kanak, J.M. Straka, R.J. Trapp, B.A. Gordon, D.S. Zrnić, G.H. Bryan, A.J. Durant, T.J. Garrett, P.M. Klein, and D.K. Lilly, 2006: The mysteries of mammatus clouds: Observations and formation mechanisms. *J. Atmos. Sci.*, **63**, 2409-2435.

Stull, R.B., 1988: *An Introduction to Boundary Layer Meteorology*. Kluwer Academic Publishers, 666 pp.

Trier, S.B. and R.D. Sharman, 2009: Convection-permitting simulations of the environment supporting widespread turbulence within the upper-level outflow of a mesoscale convective system. *Mon. Wea. Rev.*, **137**, 1972-1990.

Trier, S.B., R.D. Sharman, R.G. Fovell, and R.G. Frehlich, 2010: Numerical simulation of radial cloud bands within the upper-level outflow of an observed mesoscale convective system. *J. Atmos. Sci.*, **67**, 2990-2999.

FIGURE LEGENDS

Figure 1. Number of sondes used in this study within 100-km radial bins and 100-m vertical layers. Color shading: total number of G-IV sondes. Contours: number of G-IV sondes in Hurricane Ivan alone.

Figure 2. Vertical profile of the numerator from Eq. 1 (stability term; blue), the denominator (shear squared term; green), and the bulk Richardson number from these mean fields (red; values above 5 are set to 5). The R_B components have units 10^{-4} s^{-2}. These calculations include all G-IV sondes.

Figure 3. (a) Percentage of sondes with $R_B < 1$ as a function of height. Black: non-tropical cyclone rawinsondes. Blue: G-IV sondes within 1000 km of tropical depressions, storms and Category 1 and 2 hurricanes. Red: G-IV sondes within 1000 km of major hurricanes. (b) Same as (a), but for the percentage of $R_B \leq 0.25$. Plotted points contain a minimum of 60 observations.

Figure 4. Percentage of rawinsondes having $R_B < 1$ (blue) and < 0.25 (red), calculated from the surface to the 20 km elevation from all rawinsondes within 500 km of a major hurricane.

Figure 5. Radius-height section of the mean storm-relative radial velocity (increment 1 m s^{-1}) for Hurricane Ivan (2004), in 100-km radial bins and 100-m vertical layers. Cyan represents inflow and yellow outflow. Darker cyan and yellow indicate radial components exceeding 4 m s^{-1}.

Figure 6. Composite relative humidity with respect to ice ($T \leq 0$°C) or water ($T > 0$°C) for Hurricane Ivan (shaded). Black and red contours represent the percentage occurrence, respectively, of $R_B < 1$ (increment 15%) and $R_B < 0.25$ (stippled starting at 5%; increment 5%).

Figure 7. Two examples of turbulent layers beneath cirrus cloud base within the CDO of Hurricane Ivan. (a) and (b): infrared satellite images at the time closest to the sonde release. The X's show the release locations. Top left shows 2156 UTC 6 September 2004 and top right 2026 UTC 7 September. (c) and (d): Vertical profiles for the sondes in (a) and (b), respectively. Left panels: bulk Richardson number. Middle panels: vertical profiles of the stability term (black) and the shear squared term (green) from Eq.1. Units for both are 10^{-4} s^{-2}. Right panels: Skew T-log p diagrams for each sonde; solid blue shows temperature and dashed red shows dew point. Each long wind barb is 5 m s^{-1} and short barb 2.5 m s^{-1}. The magenta band shows the turbulent layer.

Figure 8. Composite sounding for sondes that exhibited turbulent layers beneath cirrus cloud base. Composite is with respect to the turbulent layer shown by the magenta shading. Because the turbulent layer existed over a range of heights, the composites begin at 2 km. (a) mean relative humidity with respect to ice ($T \leq 0$°C) or water ($T > 0$°C). The blue shading represents the cirrus layer. (b) mean $\partial\theta_v/\partial z$ (K km^{-1}). (c) mean storm-relative radial velocity (red) and tangential velocity (blue; both m s^{-1}). (d) R_B from Eq. 1 using the mean fields. Solid contours indicate levels where 10 or more values were available; dashed lines 4-9 sondes. No contour was plotted if fewer than 4 sonde observations were available.

Figure 9. Schematic diagram for turbulent layers beneath cloud base. The solid line represents the potential temperature from the beneath-cloud turbulence composite. Blue shading shows the cirrus layer, yellow the stable layer, and magenta the turbulent layer. The stars indicate sublimating snow or ice.

Figure 10. As in Fig. 7, but for turbulent layers in the upper troposphere produced by low stability in the absence of strong vertical wind shear. These sondes were released at 2227 UTC 6 September (a and c) and 2310 UTC 11 September (b and d).

Figure 11. Composite as in Fig. 8, but for turbulent layers in the upper troposphere within the CDO produced by low stability in the absence of strong vertical wind shear. Solid contours indicate levels where 25 or more observations were available; dashed lines 10-24 sondes. No contour was plotted if fewer than 10 sondes were available.

Figure 12. As in Fig. 7, but for high-shear turbulent layers outside the CDO. These sondes were released at 1929 UTC 8 September (a and c) and 2102 UTC 15 September (b and d).

Figure 13. Composite as in Fig. 8, but for high-shear turbulent layers outside the CDO. Solid lines indicate levels where 10 or more observations were available; dashed lines 4-9 observations.

Figure A1. Number of dropsondes that displayed saturation or supersaturation as a function of height. Blue: Hurricane Ivan (327 sondes); Red: all G-IV data (2571 sondes).

Figure A2. Black: Percentage of G-IV sondes that met the dry turbulence criterion using Eq. 1 (equivalent to the sum of the blue and red curves in Fig. 3b). Red: percentage of sondes in saturated layers that met the moist turbulence criterion (using Eq. A1 to estimate the Brunt-Väisälä frequency) when at least 26 sondes (1% of the total) were available. Blue: same, but when at least 10 sondes were available. Missing contour: fewer than 10 observations.

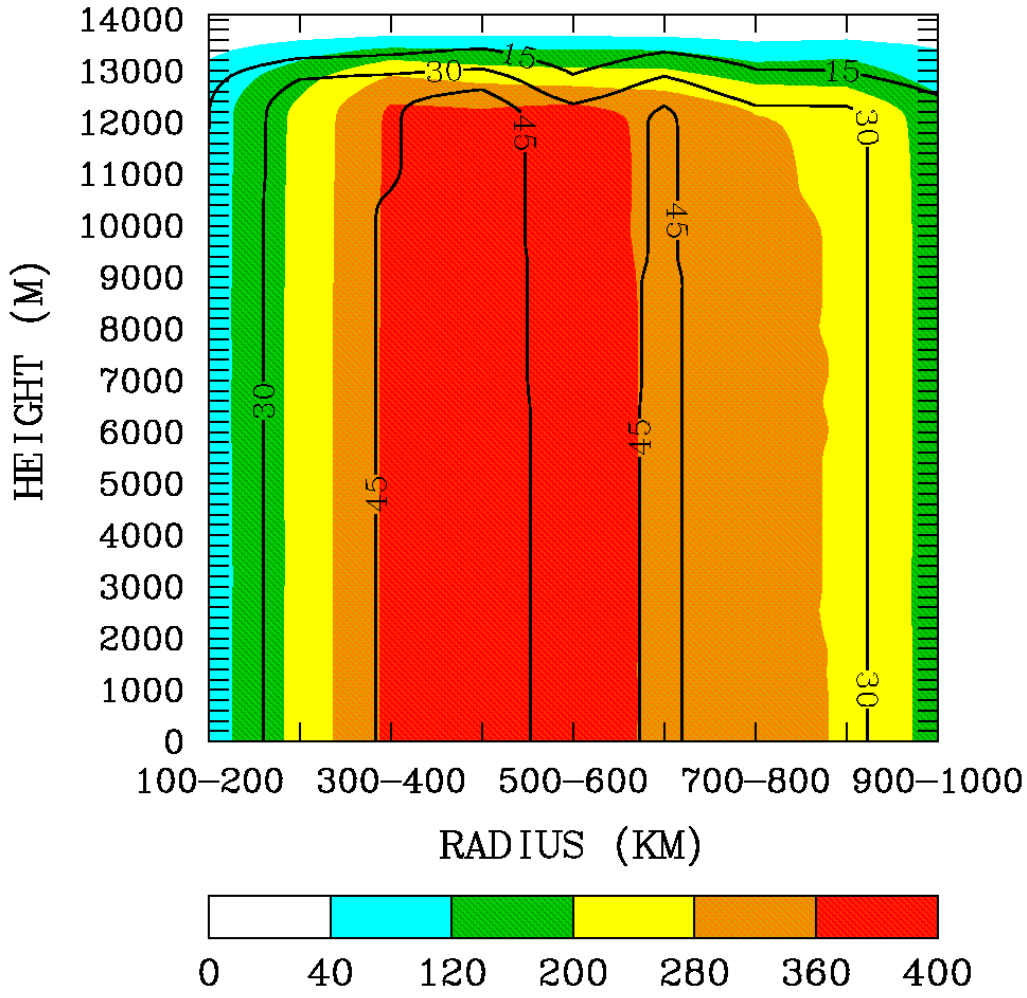

Figure 1. Number of sondes used in this study within 100-km radial bins and 100-m vertical layers. Color shading: total number of G-IV sondes. Contours: number of G-IV sondes in Hurricane Ivan alone.

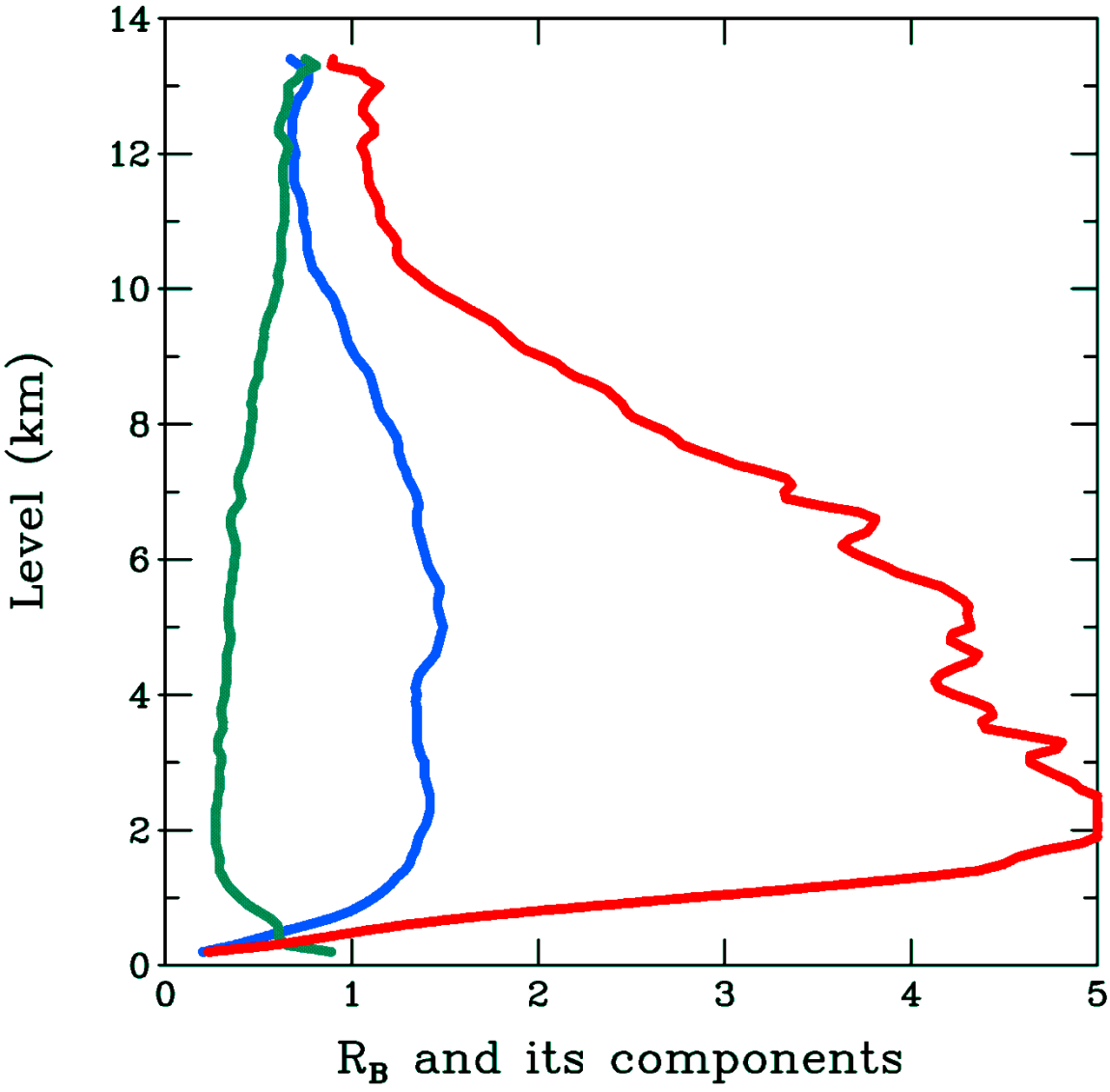

Figure 2. Vertical profile of the numerator from Eq. 1 (stability term; blue), the denominator (shear squared term; green), and the bulk Richardson number from these mean fields (red; values above 5 are set to 5). The R_B components have units 10^{-4} s^{-2}. These calculations include all G-IV sondes.

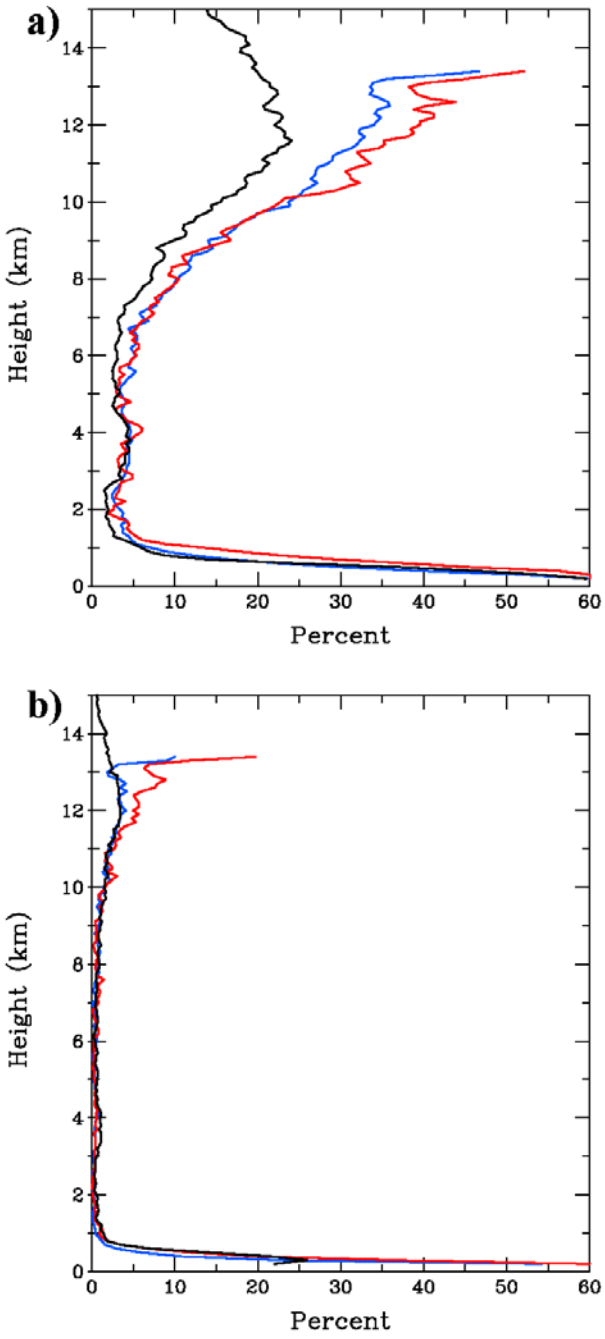

Figure 3. (a) Percentage of sondes with $R_B < 1$ as a function of height. Black: non-tropical cyclone rawinsondes. Blue: G-IV sondes within 1000 km of tropical depressions, storms and Category 1 and 2 hurricanes. Red: G-IV sondes within 1000 km of major hurricanes. (b) Same as (a), but for the percentage of $R_B \leq 0.25$. Plotted points contain a minimum of 60 observations.

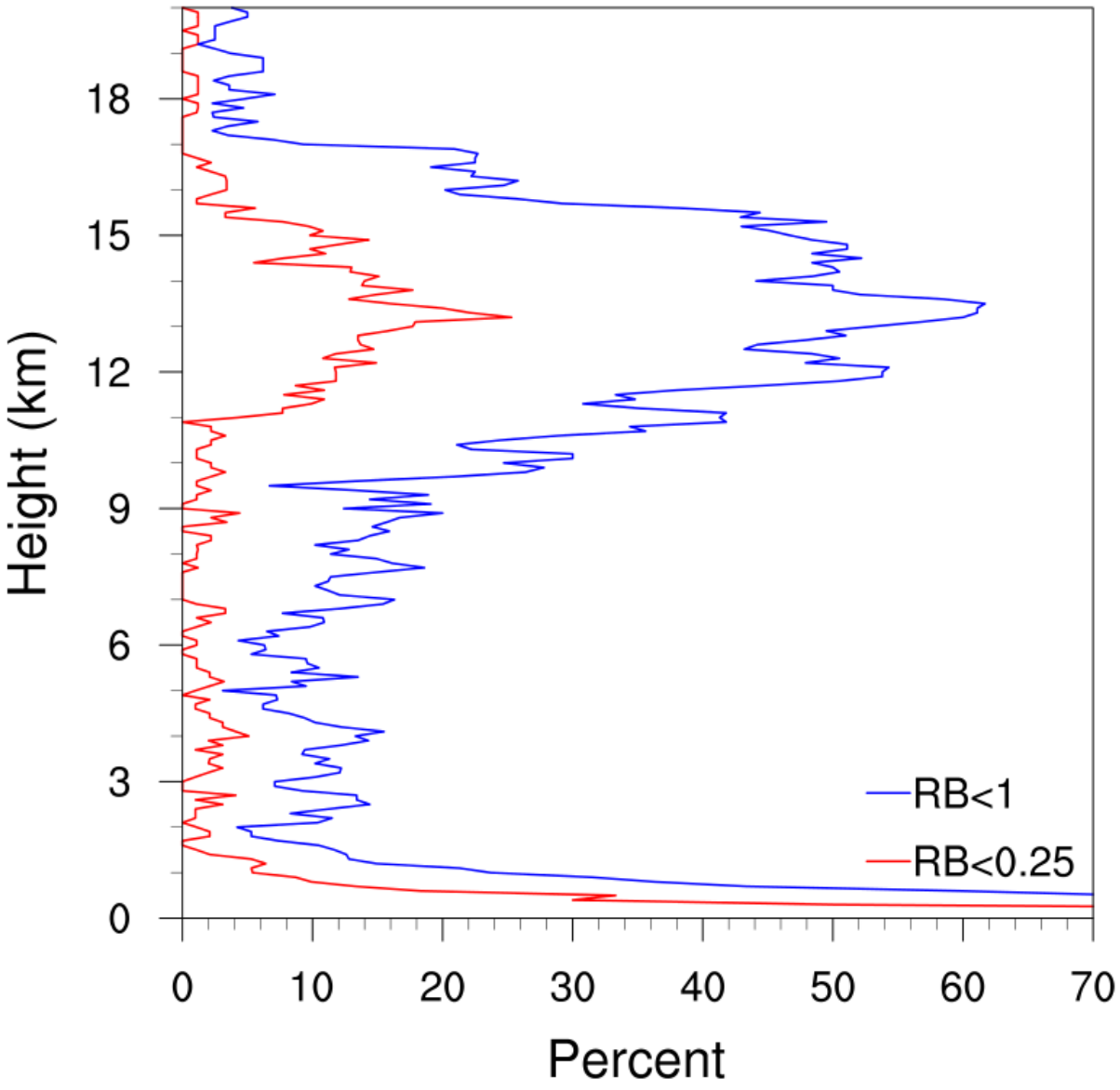

Figure 4. Percentage of rawinsondes having $R_B < 1$ (blue) and < 0.25 (red), calculated from the surface to the 20 km elevation from all rawinsondes within 500 km of a major hurricane.

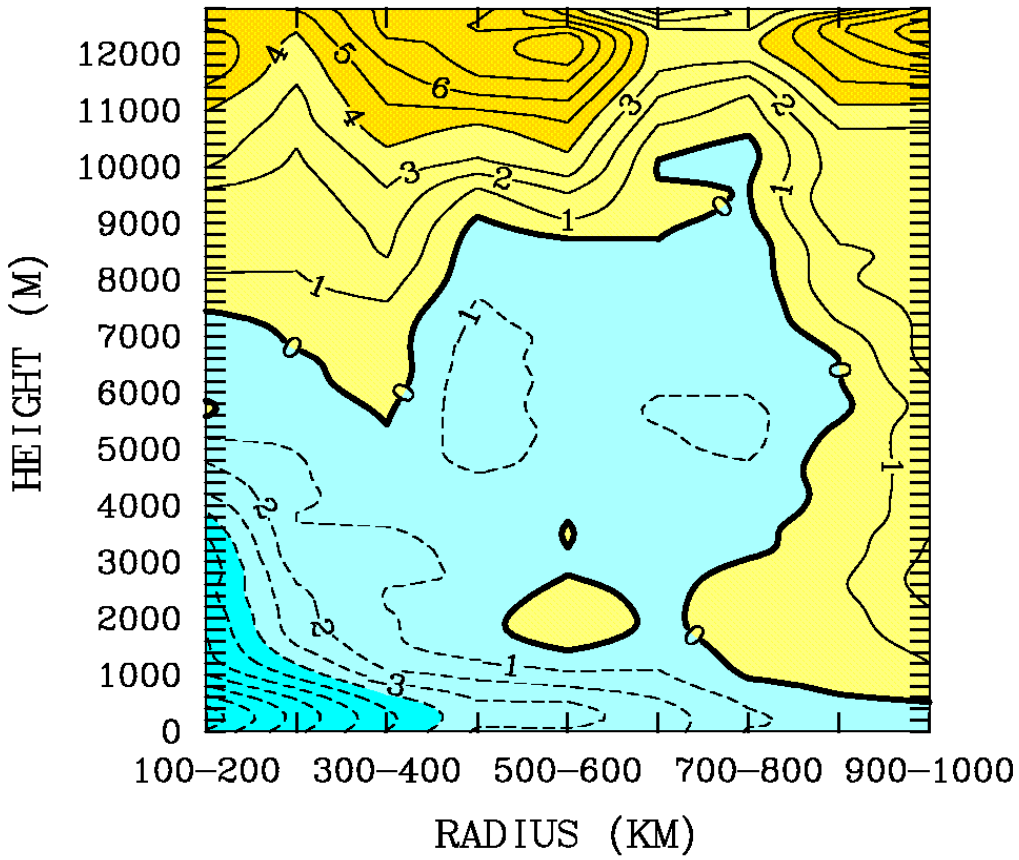

Figure 5. Radius-height section of the mean storm-relative radial velocity (increment 1 m s^{-1}) for Hurricane Ivan (2004), in 100-km radial bins and 100-m vertical layers. Cyan represents inflow and yellow outflow. Darker cyan and yellow indicate radial components exceeding 4 m s^{-1}.

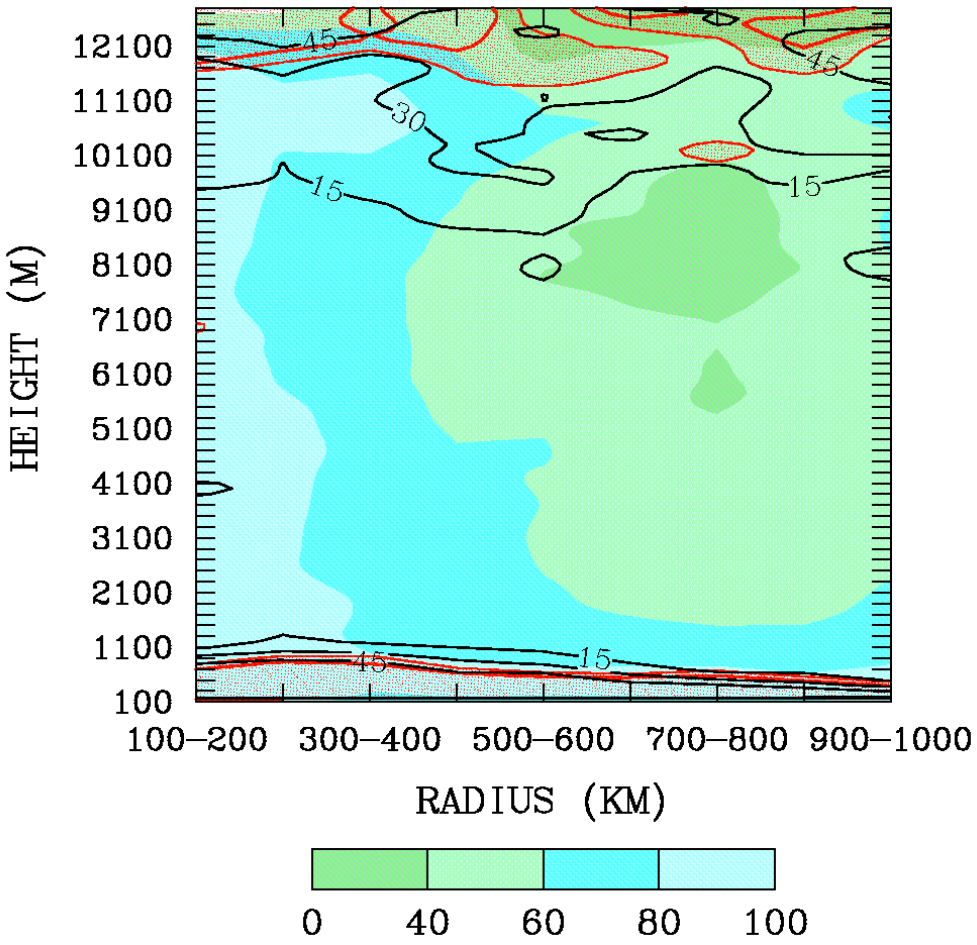

Figure 6. Composite relative humidity with respect to ice ($T \leq 0$°C) or water ($T > 0$°C) for Hurricane Ivan (shaded). Black and red contours represent the percentage occurrence, respectively, of $R_B < 1$ (increment 15%) and $R_B < 0.25$ (stippled starting at 5%; increment 5%).

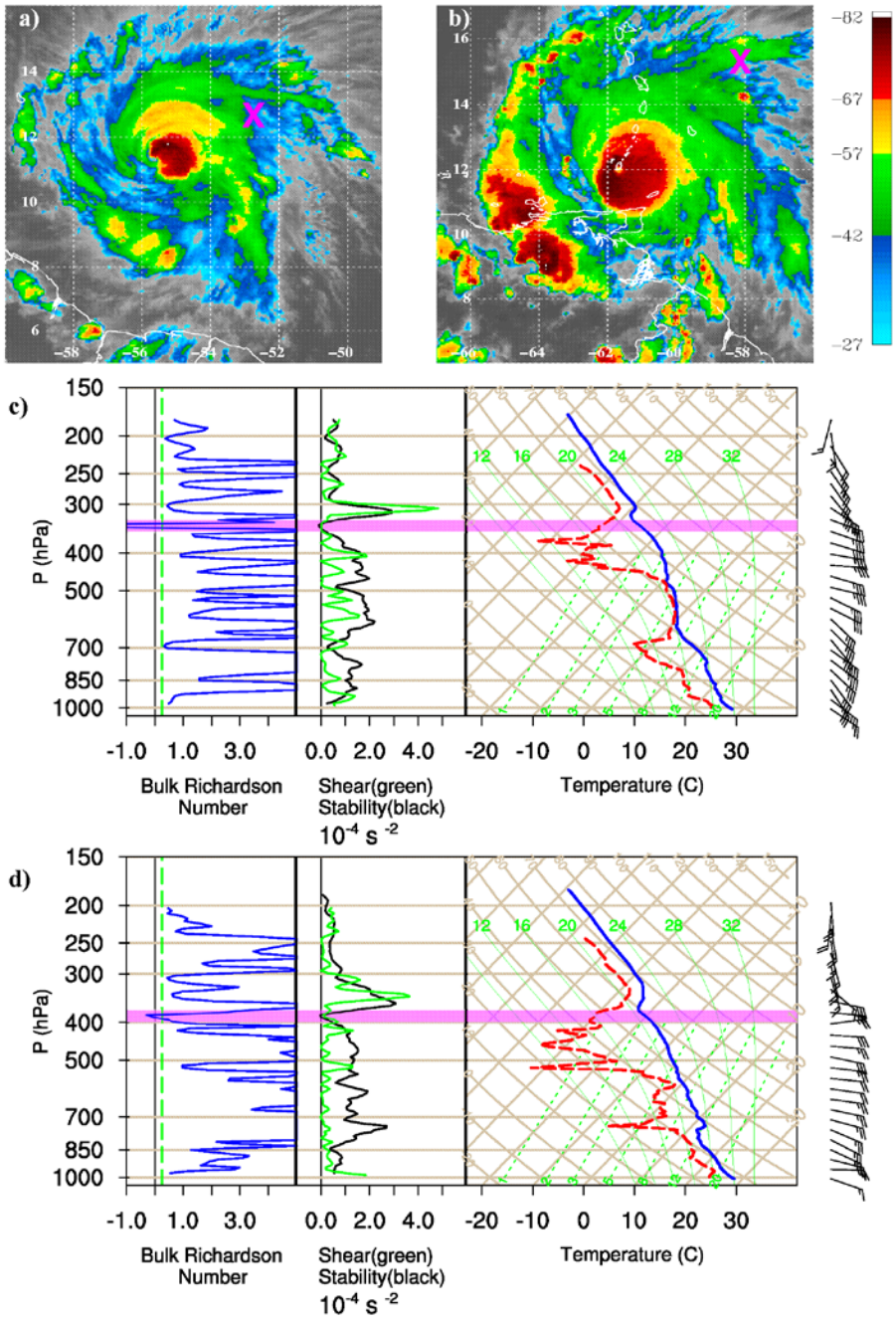

Figure 7. Two examples of turbulent layers beneath cirrus cloud base within the CDO of Hurricane Ivan. (a) and (b): infrared satellite images at the time closest to the sonde release. The X's show the release locations. Top left shows 2156 UTC 6 September 2004 and top right 2026 UTC 7 September. (c) and (d): Vertical profiles for the sondes in (a) and (b), respectively. Left panels: bulk Richardson number. Middle panels: vertical profiles of the stability term (black) and the shear squared term (green) from Eq.1. Units for both are 10^{-4} s^{-2}. Right panels: Skew T-log p diagrams for each sonde; solid blue shows temperature and dashed red shows dew point. Each long wind barb is 5 m s^{-1} and short barb 2.5 m s^{-1}. The magenta band shows the turbulent layer.

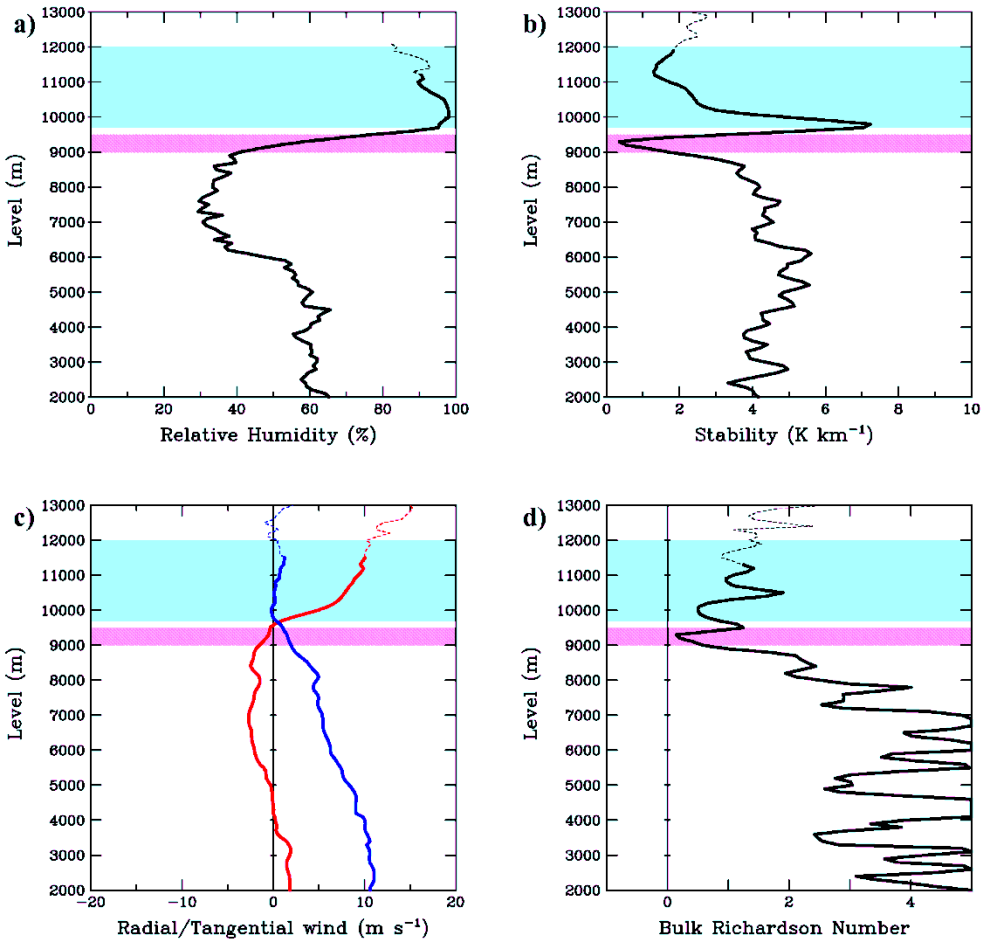

Figure 8. Composite sounding for sondes that exhibited turbulent layers beneath cirrus cloud base. Composite is with respect to the turbulent layer shown by the magenta shading. Because the turbulent layer existed over a range of heights, the composites begin at 2 km. (a) mean relative humidity with respect to ice ($T \leq 0$°C) or water ($T > 0$°C). The blue shading represents the cirrus layer. (b) mean $\partial\theta_v/\partial z$ (K km^{-1}). (c) mean storm-relative radial velocity (red) and tangential velocity (blue; both m s^{-1}). (d) R_B from Eq. 1 using the mean fields. Solid contours indicate levels where 10 or more values were available; dashed lines 4-9 sondes. No contour was plotted if fewer than 4 sonde observations were available.

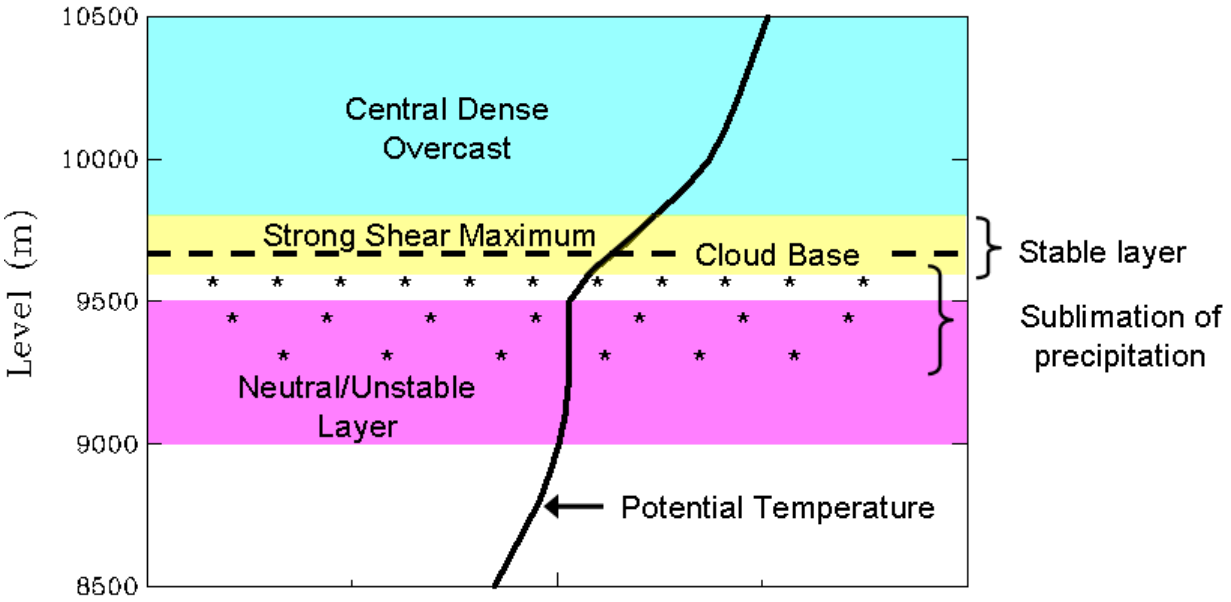

Figure 9. Schematic diagram for turbulent layers beneath cloud base. The solid line represents the potential temperature from the beneath-cloud turbulence composite. Blue shading shows the cirrus layer, yellow the stable layer, and magenta the turbulent layer. The stars indicate sublimating snow or ice.

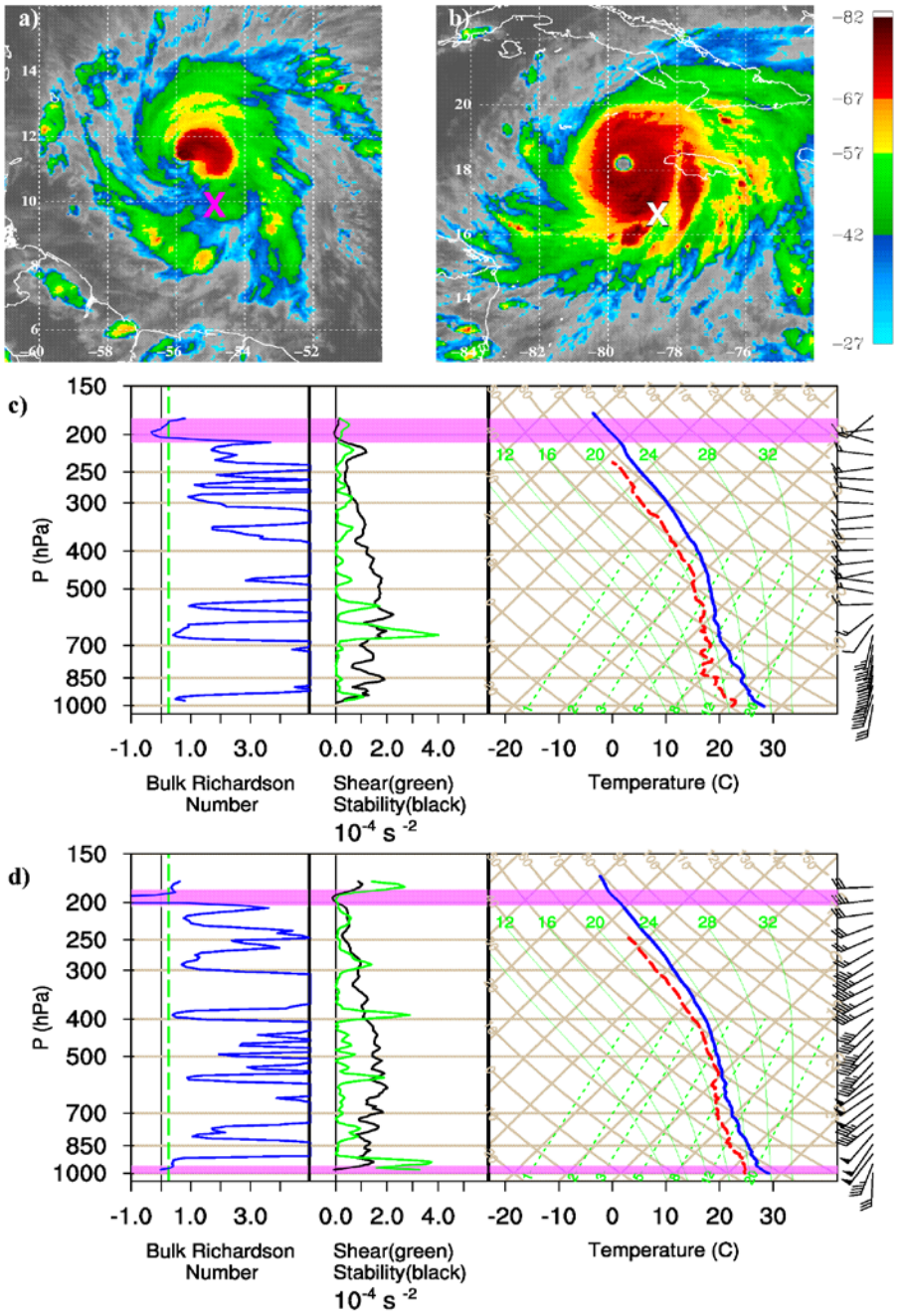

Figure 10. As in Fig. 7, but for turbulent layers in the upper troposphere produced by low stability in the absence of strong vertical wind shear. These sondes were released at 2227 UTC 6 September (a and c) and 2310 UTC 11 September (b and d).

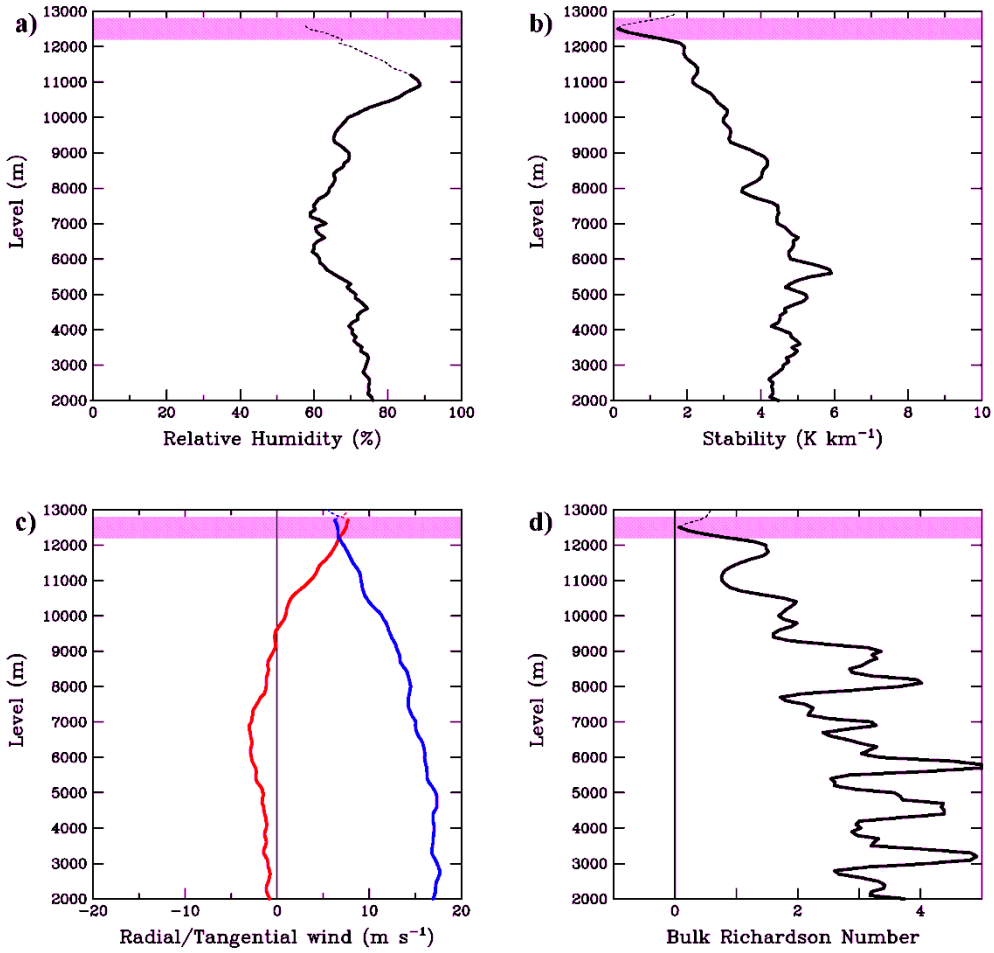

Figure 11. Composite as in Fig. 8, but for turbulent layers in the upper troposphere within the CDO produced by low stability in the absence of strong vertical wind shear. Solid contours indicate levels where 25 or more observations were available; dashed lines 10-24 sondes. No contour was plotted if fewer than 10 sondes were available.

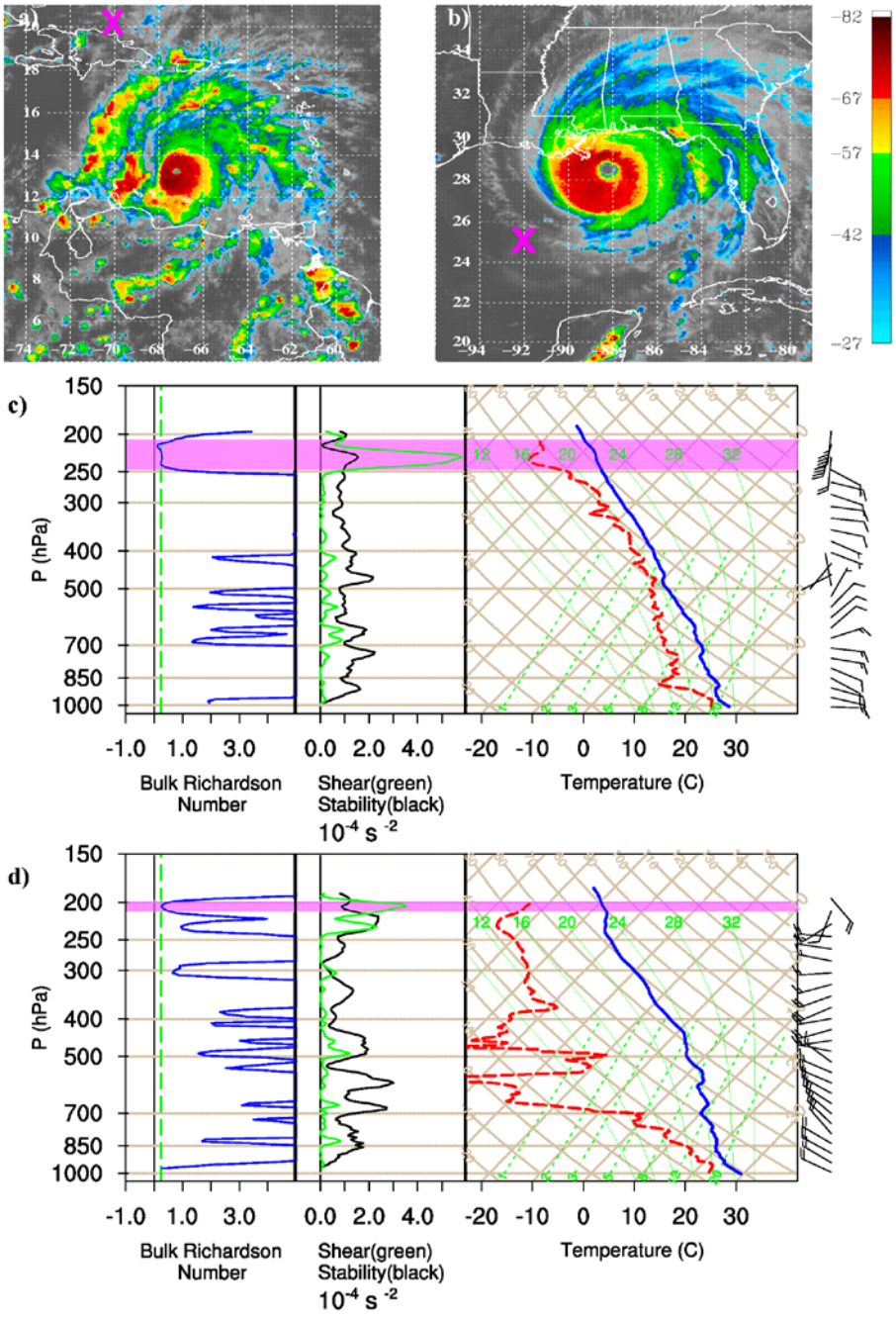

Figure 12. As in Fig. 7, but for high-shear turbulent layers outside the CDO. These sondes were released at 1929 UTC 8 September (a and c) and 2102 UTC 15 September (b and d).

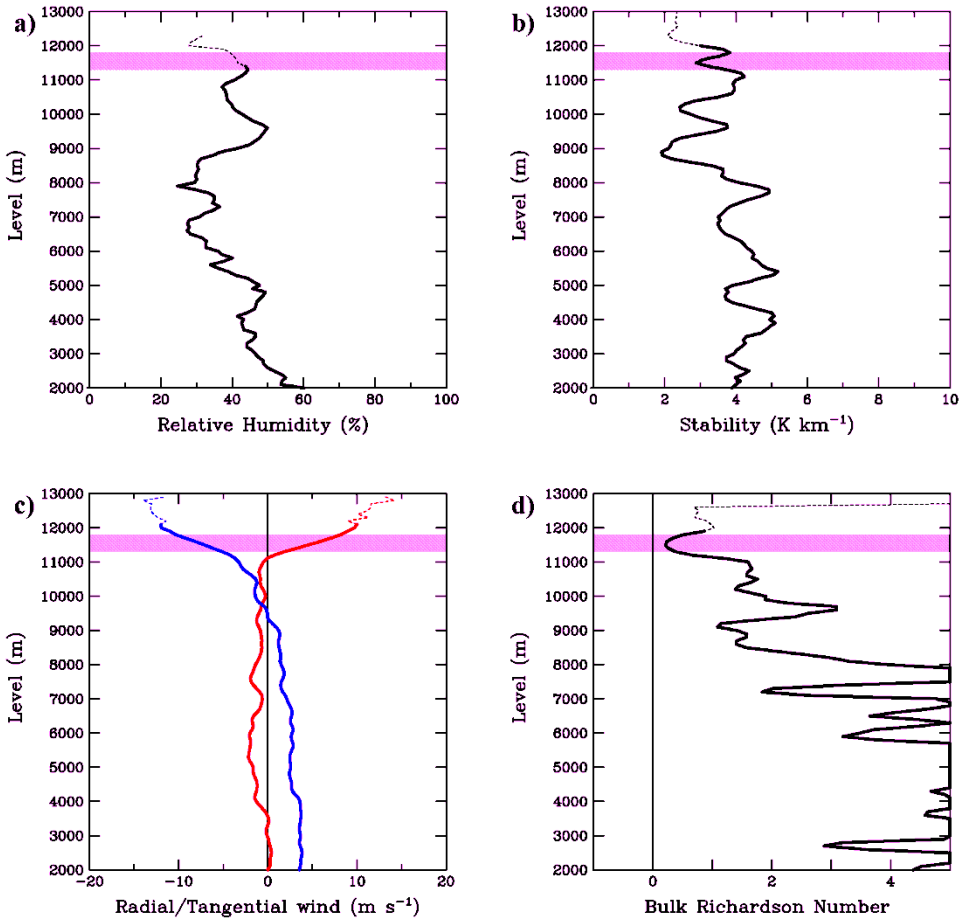

Figure 13. Composite as in Fig. 8, but for high-shear turbulent layers outside the CDO. Solid lines indicate levels where 10 or more observations were available; dashed lines 4-9 observations.

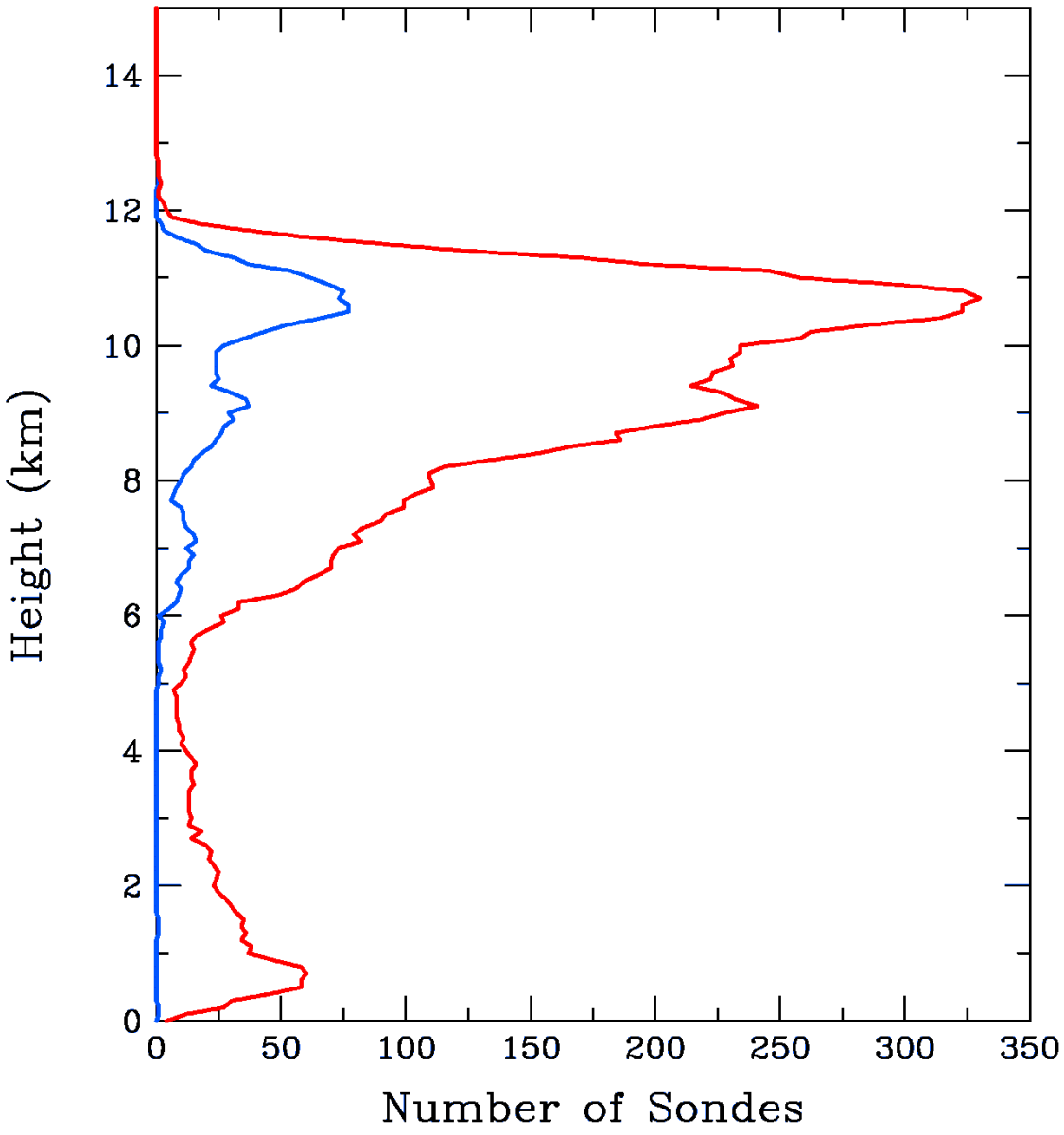

Figure A1. Number of dropsondes that displayed saturation or supersaturation as a function of height. Blue: Hurricane Ivan (327 sondes); Red: all G-IV data (2571 sondes).

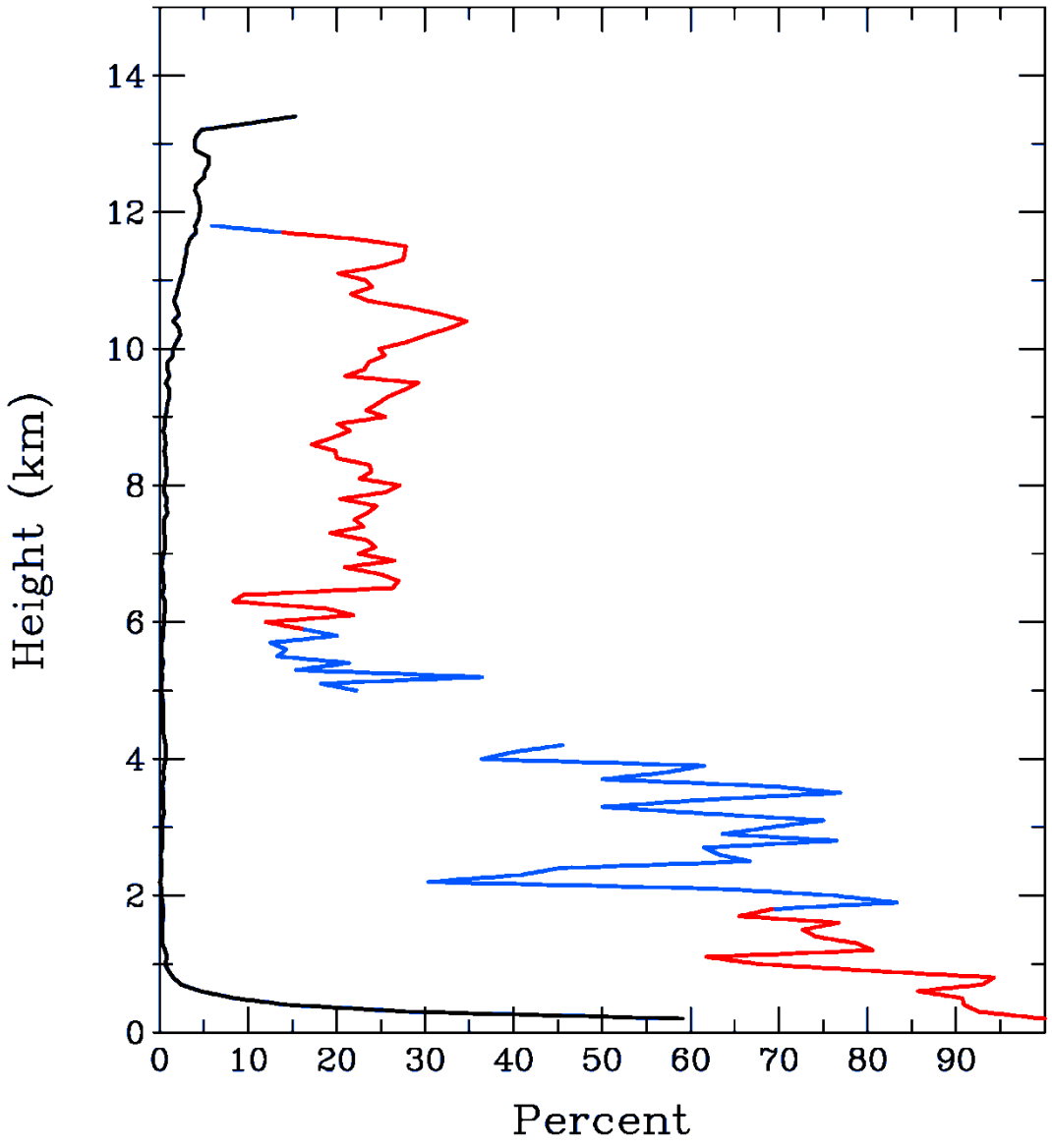

Figure A2. Black: Percentage of G-IV sondes that met the dry turbulence criterion using Eq. 1 (equivalent to the sum of the blue and red curves in Fig. 3b). Red: percentage of sondes in saturated layers that met the moist turbulence criterion (using Eq. A1 to estimate the Brunt-Väisälä frequency) when at least 26 sondes (1% of the total) were available. Blue: same, but when at least 10 sondes were available. Missing contour: fewer than 10 observations.